https://iopscience.org/ijem

SCIE, EI, SCOPUS, INSPEC, CAS, DOAJ, etc.

International Journal of Extreme Manufacturing

Precision integration of grating-based polarizers onto focal plane arrays of near-infrared photovoltaic detectors for enhanced contrast polarimetric imaging

Bo Feng, Yifang Chen, Duo Sun, Zongyao Yang, Bo Yang, Xue Li and Tao Li

Highlights:

- A number of fundamental technical problems in scaling up by monolithically integrating grating-based polarizers onto a focal plane array (FPA) of infrared detectors were successfully solved.
- Polarimetric and photovoltaic chips with divisions of the focal plane of 540 × 4 pixels and 300 × 256 superpixels were successfully manufactured. Polarimetric imaging with enhanced contrast was demonstrated.
- A broad avenue toward industrialization of high quality polarimetric imaging in infrared wavelengths was opened up.

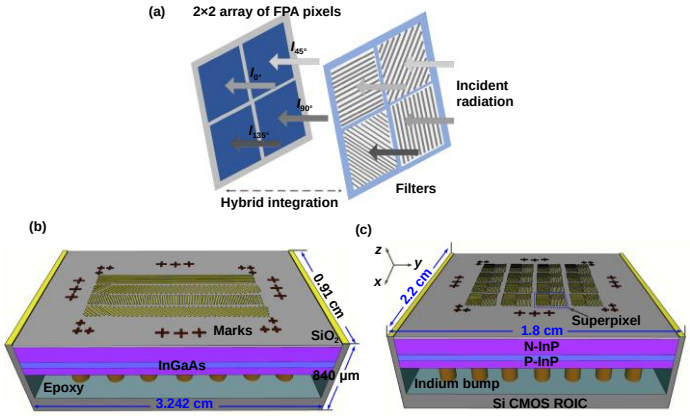

View online: https://iopscience.iop.org/article/10.1088/2631-7990/abf5c8

Article Download:https://iopscience.iop.org/article/10.1088/2631-7990/abf5c8/pdf

Citation: Feng B, Chen Y F, Sun D, Yang Z Y, Yang B et al. Precision integration of grating-based polarizers onto focal plane arrays of near-infrared photovoltaic detectors for enhanced contrast polarimetric imaging. *Int. J. Extrem. Manuf.* **3**, 035201(2021).

Related articles:

Laser synthesis and functionalization of nanostructures

Costas P. Grigoropoulos

Citation: Grigoropoulos C P. Laser synthesis and functionalization of nanostructures. *Int. J. Extrem. Manuf.* **1**, 012002 (2019).

At wavelength coherent scatterometry microscope using high-order harmonics for EUV mask inspection

Yutaka Nagata, Tetsuo Harada, Takeo Watanabe, Hiroo Kinoshita and Katsumi Midorikawa

Citation: Nagata Y, Harada T, Watanabe T, Kinoshita H, Midorikawa K. At wavelength coherent scatterometry microscope using high-order harmonics for EUV mask inspection. *Int. J. Extrem. Manuf.* **1**, 032001 (2019).

Scanning probe lithography on calixarene towards single-digit nanometer fabrication

Marcus Kaestner and Ivo W Rangelow

Citation: Kaestner M, Rangelow I W. Scanning probe lithography on calixarene towards single-digit nanometer fabrication. *Int. J. Extrem. Manuf.* **2**, 032005 (2020).

Directed self-assembly of block copolymers for sub-10 nm fabrication

Yu Chen and Shisheng Xiong

Citation: Chen Y, Xiong S S. Directed self-assembly of block copolymers for sub-10 nm fabrication. *Int. J. Extrem. Manuf.* **2**, 032006 (2020).

OPEN ACCESS
IOP Publishing | IMMT
International Journal of Extreme Manufacturing
Int. J. Extrem. Manuf. 3 (2021) 035201 (8pp)
https://doi.org/10.1088/2631-7990/abf5c8

Precision integration of grating-based polarizers onto focal plane arrays of near-infrared photovoltaic detectors for enhanced contrast polarimetric imaging

Bo Feng[1], Yifang Chen[1,*], Duo Sun[2], Zongyao Yang[1], Bo Yang[2], Xue Li[2] and Tao Li[2,*]

[1] Nanolithography and Application Research Group, State Key Laboratory of ASIC and System, School of Information Science and Technology, Fudan University, Shanghai 200433, People's Republic of China
[2] State Key Laboratories of Transducer Technology, Shanghai Institute of Technical Physics, Chinese Academy of Sciences, Shanghai 200083, People's Republic of China

E-mail: yifangchen@fudan.edu.cn and litao@mail.sitp.ac.cn

Received 1 July 2020, revised 2 December 2020
Accepted for publication 7 April 2021
Published 30 April 2021

Abstract

Polarimetric imaging enhances the ability to distinguish objects from a bright background by detecting their particular polarization status, which offers another degree of freedom in infrared remote sensing. However, to scale up by monolithically integrating grating-based polarizers onto a focal plane array (FPA) of infrared detectors, fundamental technical obstacles must be overcome, including reductions of the extinction ratio by the misalignment between the polarizer and the detector, grating line width fluctuations, the line edge roughness, etc. This paper reports the authors' latest achievements in overcoming those problems by solving key technical issues regarding the integration of large-scale polarizers onto the chips of FPAs with individual indium gallium arsenide/indium phosphide (InGaAs/InP) sensors as the basic building blocks. Polarimetric and photovoltaic chips with divisions of the focal plane of 540 × 4 pixels and 320 × 256 superpixels have been successfully manufactured. Polarimetric imaging with enhanced contrast has been demonstrated. The progress made in this work has opened up a broad avenue toward industrialization of high quality polarimetric imaging in infrared wavelengths.

Supplementary material for this article is available online

Keywords: polarimetric imaging, grating based polarizer, InGaAs/InP, focal plane array, nanofabrication

1. Introduction

Extensive applications of polarimetric detection in infrared wavelengths can be found in climate observation, environmental monitoring, space science/technology, security, and submarine imaging [1–18]. Several techniques have been reported to realize polarization imaging, including divisions of time, amplitude, focal plane, and aperture [19]. Our earlier work has demonstrated that subwavelength metallic gratings acting as polarizers integrated with an indium gallium arsenide/indium phosphide (InGaAs/InP) focal plane array (FPA) in the division of the focal plane (DoFP) exhibit great advantages, such as high quantum efficiency and low dark current at room temperature operation [19–25]. However, in the scale up for integration of subwavelength metallic gratings

* Authors to whom any correspondence should be addressed.

2631-7990/21/035201+8$33.00

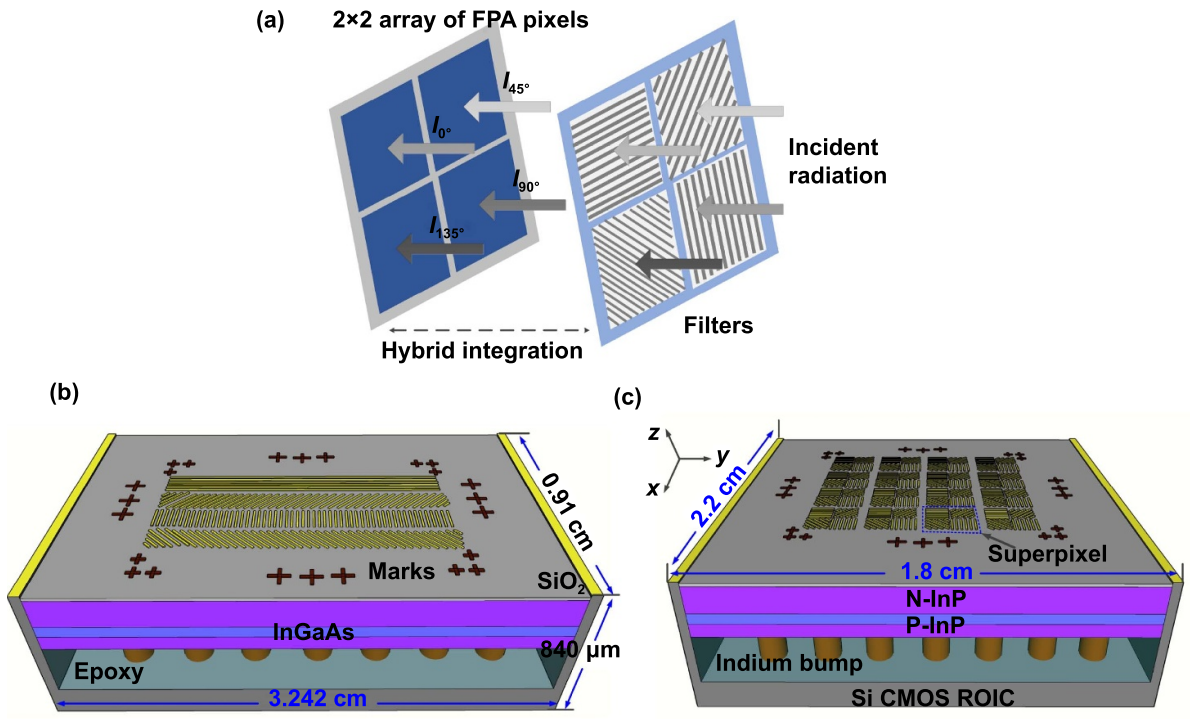

Figure 1. Schematics of the devices fabricated in this work. (a) A polarization filter array and a FPA sensor comprising an imaging polarimeter by the division-of-focal-plane modulation scheme; and (b), (c) the specially designed grating-based polarizers with the InGaAs/InP detectors by DoFP with 540 × 4 pixels and 320 × 256 superpixels.

with an FPA of 540 × 4 pixels and 320 × 256 superpixels (each pixel contains four subpixels with four different polarization orientations) by electron beam lithography (EBL), a number of key technical problems must be addressed before the fabricated polarization FPA is able to demonstrate polarimetric imaging with enhanced contrast.

First, the misalignment of the gratings with the detector array may lead to dramatic reduction of the extinction ratio of the fabricated polarimetric detector (ratio of the maximum to minimum value of the electronic signal), according to our earlier results [19]. Highly precise alignment is required. Second, the line-width, in association with the duty ratio (grating line-width/space), can significantly influence the extinction ratio of polarizers, i.e. the ratio of the transmittances between the cross-polarized light and the parallel polarized light as discovered in our previous work [23, 24]. In replicating gratings with either an orientation of 45° or 135° by EBL, diagonal lines (45° or 135°) are always narrower than the horizontal or the vertical lines, due to the difference in grid resolution between the orthogonal and the diagonal orientations, leading to nonuniform transmission. Third, it was first found in our work that the line edge roughness (LER) is also significantly responsible for the decrease in the extinction ratio of polarizers. Although the origin of the LER effect on the extinction is still under investigation, effective measures must be taken to eliminate the LER as much as possible to maintain a high extinction ratio. Therefore, to break through those fundamental obstacles, an innovative technique must be developed to overcome a number of vital issues in the scaling up of the infrared FPA of polarization detectors.

This paper reports our technical progress in monolithic integration of uniform aluminum (Al) subwavelength gratings as the polarizers with 540 × 4 pixelated and 320 × 256 superpixelated FPAs of InGaAs/InP detectors by the mix-and-match of ultraviolet (UV) exposure/EBL through a highly precise registration technique. Optimized parameters in sample-size-compatible EBL and reduction of the LER of Al gratings has been worked out to ensure a highly accurate alignment and high extinction ratio in the polarimetric performance. Initial results with the enhanced contrast quality of the infrared imaging in 0.9–1.7 μm by the fabricated chips have been obtained. The solutions to the technical difficulties encountered in this work should be beneficial for the monolithic integration of subwavelength gratings with the FPA of detectors in an even larger scale.

2. Methods

2.1. Design of InGaAs/InP-based polarimetric detectors

A typical DoFP method was adopted by using the Bayer pattern with four subwavelength gratings at an orientation of 0°, 45°, 90° and 135°, to calculate the first three Stokes vectors, as schematically illustrated in figure 1(a). The Stokes parameters were reconstructed based on the intensity measurements by equation (1) [5]:

$$S = \begin{bmatrix} S_0 \\ S_1 \\ S_2 \\ S_3 \end{bmatrix} = \begin{bmatrix} \langle |E_x|^2 + |E_y|^2 \rangle \\ \langle |E_x|^2 - |E_y|^2 \rangle \\ 2\,\mathrm{Re}\,\langle E_x E_y^* \rangle \\ -2\,\mathrm{Im}\,\langle E_x E_y^* \rangle \end{bmatrix} \alpha \begin{bmatrix} I_0 + I_{90} \\ I_0 - I_{90} \\ I_{45} - I_{135} \\ I_L - I_R \end{bmatrix} \quad (1)$$

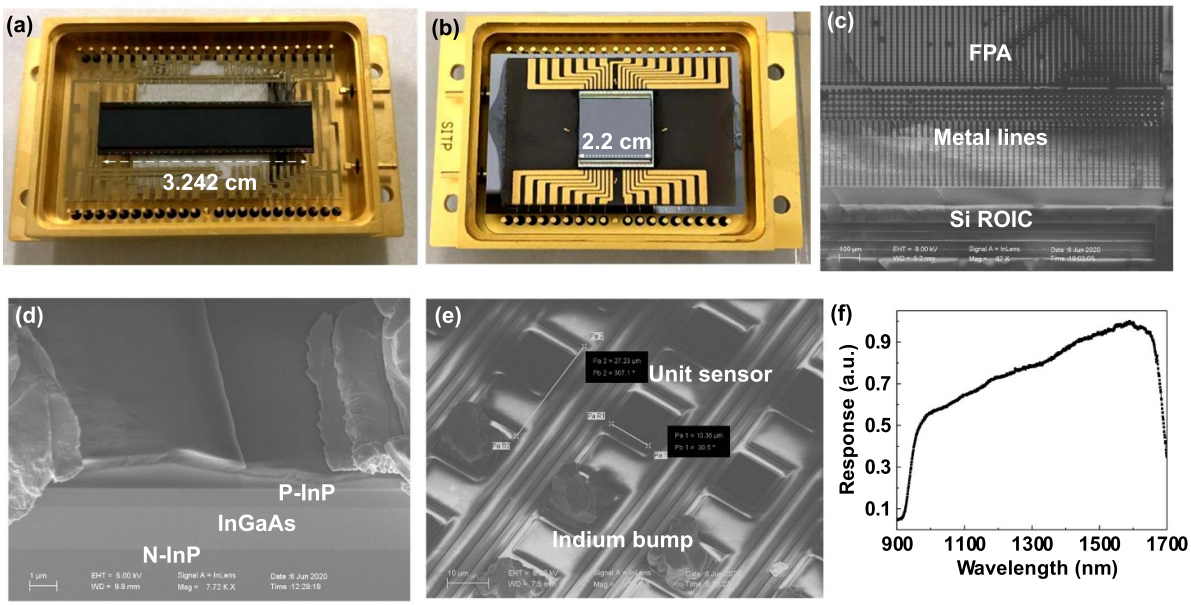

Figure 2. The prefabricated InGaAs/InP FPA detectors with different sample scales. (a) 540 × 4 pixels detector, whose wafer dimensions were 3.242 cm in length and 0.91 cm in width; and (b) 320 × 256 superpixels detector, whose wafer dimensions were 2.2 cm in length and 1.8 cm in width; (c)–(e) photos of the device by a scanning electron microscope (SEM); and (f) the measured response spectrum of an individual detector.

where S_0 is the total intensity of the light, S_1 is the difference between horizontal and vertical polarization, and S_2 is the difference between linear 45° and 135° polarization.

The InGaAs/InP-based FPA with 540 × 4 pixels, integrated with metallic grating polarizers for detection in near infrared wavelengths, is schematically shown in figure 1(b). Backside-illuminated InGaAs FPA sensing pixels reduced the space between the polarizer and the photodiode, therefore, eliminated the likelihood of crosstalk, where an incident light passes through the filter of one pixel but is registered by an adjacent pixel. Since the polarizer to be integrated was composed of four groups of linear arrays of subwavelength Al gratings, each of which had a specific orientation of 0°, 45°, 90° and 135°, the target chip was able to gain a large view of the field for polarization imaging by a push-broom scanning pattern [20]. Figure 1(c) depicts a 320 × 256-superpixel-structured polarimetric InGaAs FPA in which each superpixel consists of 2 × 2 Al gratings with four different angles, similar to the well-known Bayer pattern. The polarization FPA detector with superpixels was able to determine the degree and the angle of linear polarization of the image. A sufficient number of sensing pixels at both the *x*-axis and *y*-axis directions also made it meet staring imaging patterns [19]. Meanwhile, all of the polarimetric FPAs can acquire the near-infrared spectral and polarization characteristics of the imaged object in real time to significantly enhance the image contrast.

2.2. Prefabrication of InGaAs/InP FPA detectors

The prefabricated InGaAs/InP-based FPA detector with 540 × 4 pixels (wafer dimensions: 3.242 cm in length and 0.91 cm in width) is presented in figure 2(a); and the InGaAs/InP-based FPA detector with 320 × 256 superpixels (wafer dimensions: 2.2 cm in length and 1.8 cm in width) is presented in figure 2(b). Both detectors mainly consist of an InGaAs photosensitive chip interconnected with silicon (Si) complementary metal oxide semiconductor (CMOS) read-out circuits (ROICs). The $In_{0.53}Ga_{0.47}As$/InP FPA photosensitive chip has the layer structure of a 350 μm-thick InP substrate covered by a 200 nm thick *N*-type InP buffer layer, then a 2.5 μm-thick, unintentionally doped InGaAs absorption layer, finished by a 1 μm *P*-type InP layer formed by the thermal diffusion of zinc (Zn) into InP. The Si-based CMOS ROIC was electrically interconnected with a photosensitive chip via the indium bumps flip-chip bonding technique for reading electrical signals. The area and the pitch of each sensing pixel was 11 μm and 30 μm. The details are depicted in figures 2(c)–(e). A 200 nm thick silicon dioxide (SiO_2) dielectric layer was then back grown on the conventional InP substrate by inductively coupled plasma chemical vapor deposition, which was essential for the metallic subwavelength gratings to act as a polarizer in the infrared wavelength for a high extinction ratio [22]. Figure 2(f) depicts the measured normalized response spectrum of the InGaAs FPA. The response wavelength ranged between 0.9 and 1.7 μm, and the peak responsivity was as high as up to 0.71 A W^{-1} at 1.55 μm, corresponding to a quantum efficiency of 56.8%. The detectivity of photosensitive elements was ~1.95 × 10^{12} cm $Hz^{1/2}$/W at room temperature.

3. Experiments and results

3.1. Integration of metallic gratings directly onto InGaAs/InP detectors

In the integration of the subwavelength gratings onto the FPA of InGaAs/InP detectors, a mix-and-match technique was applied, i.e. a UV exposure by a mask aligner (SUSS

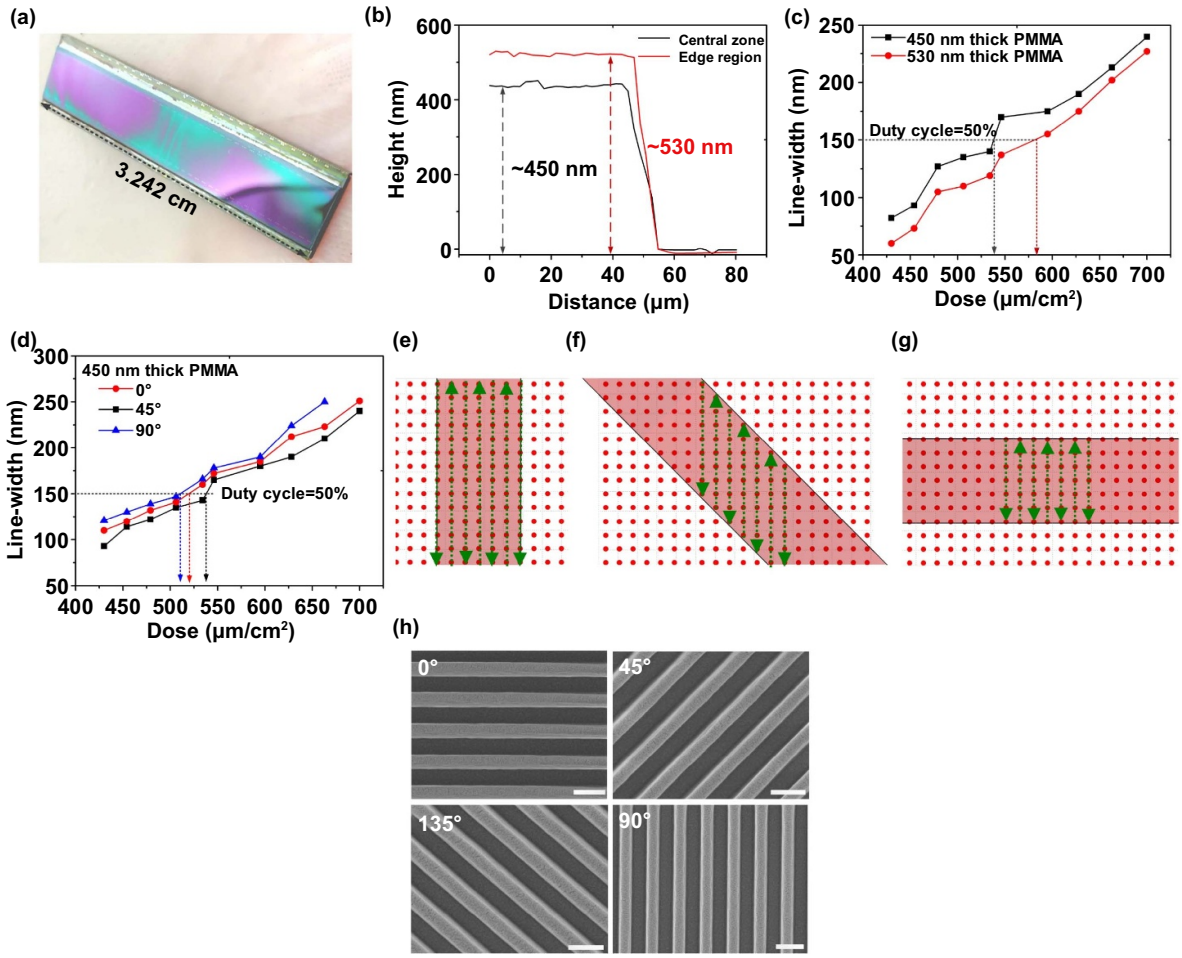

Figure 3. The technical issues related to the line-width control. (a) The optical image of spin-coated, uneven PMMA with different colors, indicating the thickness fluctuations throughout the rectangular wafer; (b) the AFM-measured PMMA thickness in the central and the edge region; (c) the resultant line width vs. the exposure dose in two different regions with different PMMA thicknesses for the 45° oriented grating; (d) the line width with three different orientations of the lines on the 450 nm thick PMMA; (e)–(g) the schematic diagrams show the differences of the writing grid densities on the line edges for the three different orientations of grating; and (h) the SEM photos of fabricated 0°, 45°, 90° and 135° orientated gratings with a consistent 150 nm line width and 300 nm pitch in uneven PMMA resist (scaling bar, 300 nm).

MA6) was carried out for both detectors and alignment marks simultaneously, which would be used in EBL for sub-wavelength gratings. The alignment mark consisted of 20 nm titanium (Ti)/100 nm platinum (Pt) on the top of a SiO_2 layer (figure 1(b)), in which the Ti layer acted as an adhesion. In replicating the metallic gratings, EBL was carried out by a JEOL 6300 FS system with a beam of 7 nm spot size and 500 pA beam current at 100 KeV to generate equal line/space patterns in polymethyl methacrylate (PMMA) (MW350K) for Al pixel/superpixel gratings. The precise mounting of the sample with a rectangular shape (3.242 cm in length and 2.2 cm in width) to the standard holder of the JEOL beam writer was extremely critical to the e-beam focusing and alignment accuracy. As mentioned in the introduction, a small misalignment between the polarizer and the sensor area may cause a big loss of extinction ratio for fabricated polarimetric detectors. A specially designed sample-size-compatible procedure was developed to realize the precise integration of grating based polarizers directly onto FPAs (see figure S1, Supporting information (available online at stacks.iop.org/IJEM/3/035201/mmedia)).

In this work, the line width, the pitch, and the thickness of the subwavelength Al gratings to be integrated was fixed at 150 nm, 300 nm, and 100 nm, based on the design in our earlier work [19, 20]. A 450 nm thick PMMA (MW350K) was first spin coated and then baked on a hot plate at 110 °C for 8 min. Due to the rectangular shape of the wafers, the thickness of the PMMA layer was uneven, as can been seen by various colors on the coated sample in figure 3(a). The thickness difference was measured by an atomic force microscope (AFM) supplied by Bruker, as shown in figure 3(b). The PMMA thickness was measured to be 450 nm in the center and 530 nm on the edge of the sample. With such a deviation in resist thickness, it was rather difficult to achieve a consistent line-width (150 nm) from site to site. To solve this problem, the dependence of the line-width on the exposure dose at different PMMA thickness was first characterized, as shown in figure 3(c). To maintain a constant duty cycle (50%) throughout the 300 nm

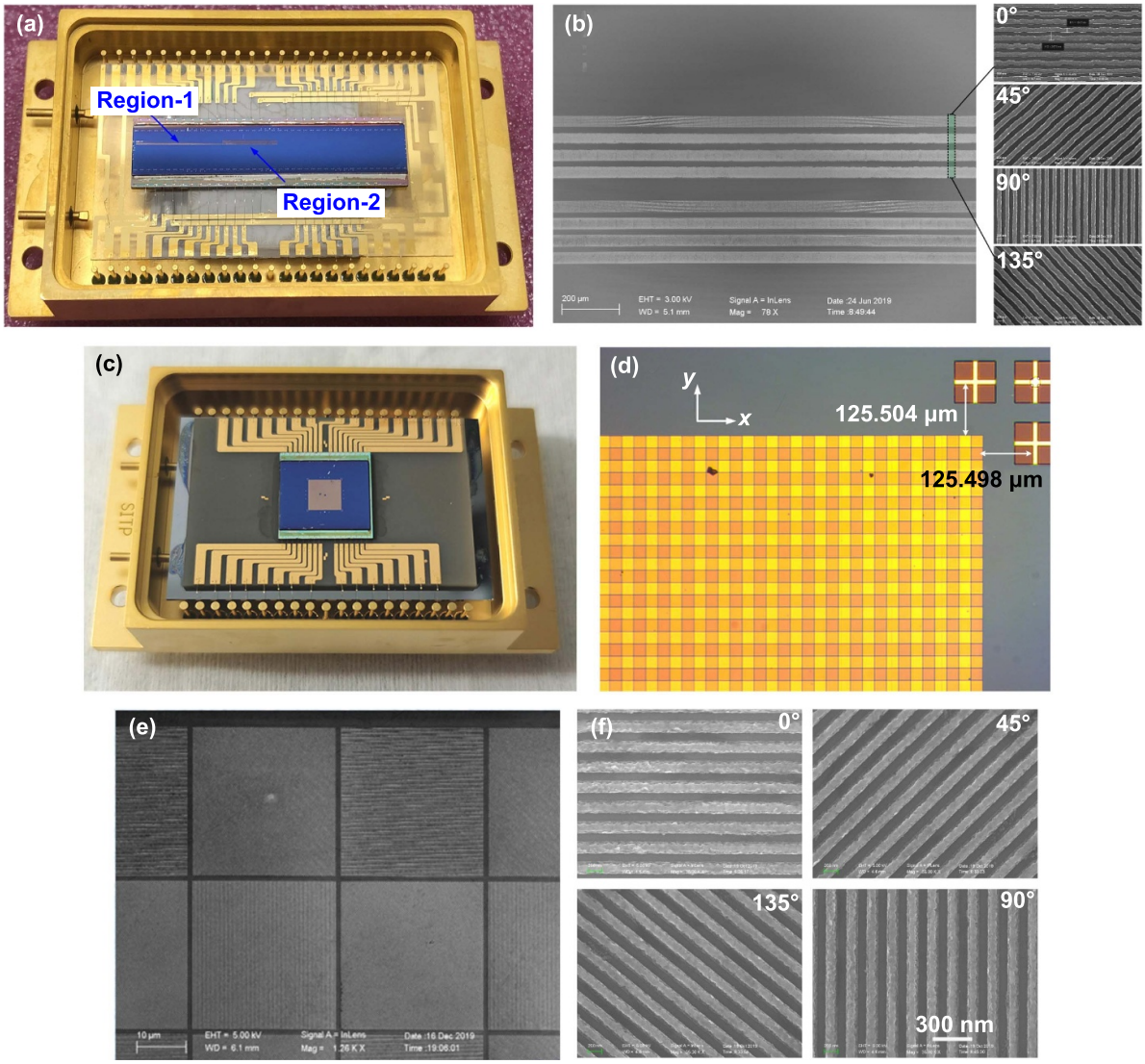

Figure 4. The successfully integrated photoelectronic chips in near infrared wavelengths. (a), (b) The 3.242 cm long FPA of 540 × 4 pixelated conventional InGaAs/InP detectors, integrated with Al grating-based polarizers. (c)–(e) The 2.2 cm long FPA of 320 × 256 superpixelated detectors integrated with grating-based polarizers.

pitched Al gratings to ensure the same transmission of each polarizer with minimized extracting errors for the Stokes parameters, a higher exposure dose (580 μC cm^{-2}) was applied for the 530 nm thick PMMA than that with a 450 nm thickness (537 μC cm^{-2}). The change in the line-width from 60 nm to 240 nm with the exposure dose from 430 to 700 μC cm^{-2}, as presented in figure 3(c), also indicated the excellent line width control of the process with a broad dose window.

Another equally important issue related to the line width control in EBL is the grating line orientation effect on the line width. There are a total of four gratings in one superpixel, each of them orientated at 0°, 45°, 90° and 135°, to the horizontal direction, i.e. 0°. Dose tests of the line width against the exposure doses for three different orientation angles of the gratings, i.e. 0°, 45° and 90°, to the horizon were carried out; and the results are presented in figure 3(d). Clearly, when exposed by the same dose, the vertically oriented grating gave rise to the widest lines, the one with diagonal lines gave rise to the narrowest lines, and the one with horizontally oriented lines had a line width in between the other two gratings. The line width deviations between different oriented gratings were caused by the differences in writing grid density along the lines, as schematically illustrated in figures 3(e)–(g). The red dots represent the e-beam writing grids. Comparing the diagonal lines (figure 3(f)) with the vertical (figure 3(e)) or horizontal lines (figure 3(g)), it had the lowest grid density on the line edge, leading to the reduced exposure dose. Although the grid density on the line edges of both the vertical and horizontal gratings were identical, the LER of the horizontal grating was larger than that of the vertical one because the e-beam writing trace of the JEOL 6300 FS was vertical, as shown by the dashed lines with green color, which was in line with the vertical grating, causing relatively low edge roughness.

Taking the grating orientation effect into account, three different base doses (537 μC cm^{-2}, 520 μC cm^{-2} and 508 μC cm^{-2}) were used for the exposures of the three

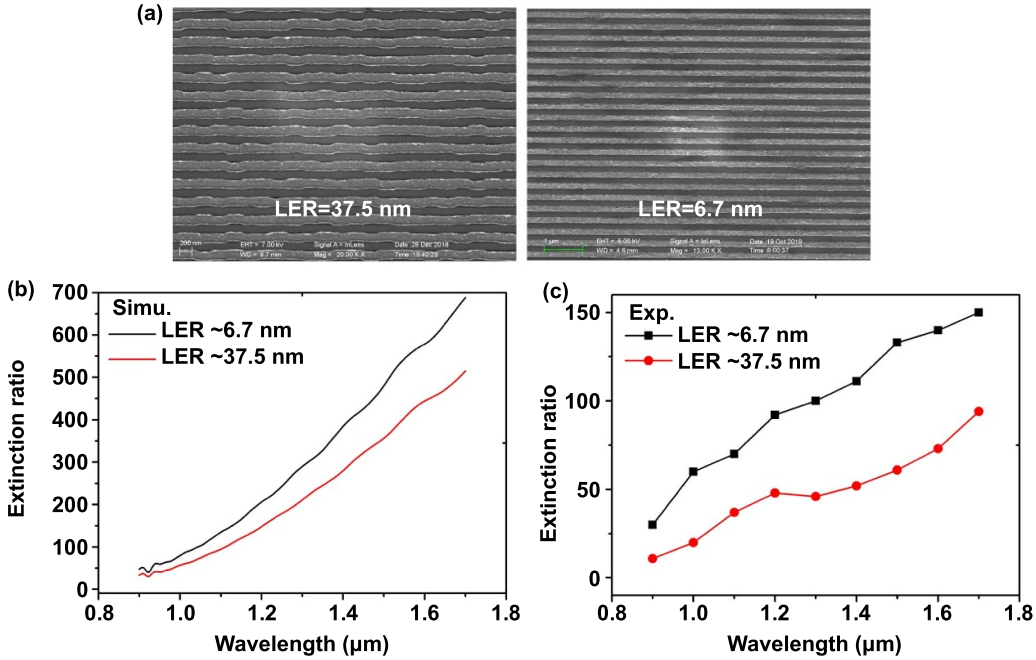

Figure 5. The effect of the LER on the polarization property. (a) The fabricated metallic Al gratings with an LER of 37.5 nm and 6.7 nm, respectively, on the 200 nm SiO_2 coated on a 350 μm thick InP substrate. The comparison of the extinction ratios in near infrared wavelengths from the two Al gratings was obtained by the FDTD simulation (b) and the measured results (c). Both the theoretical and experimental results showed the LER may deteriorate the polarization performance.

orientated gratings in the layout (figure S2, supporting information). Furthermore, to overcome the problem of the uneven thickness of PMMA in different regions on the 540 × 4 FPAs with a wafer length of 3.242 cm, as mentioned above, the sample area was divided into two regions according to the PMMA thicknesses, from 450 nm to 530 nm (figure S2(a), supporting information). EBL was carried out by using the corresponding doses to ensure the grating line-width was consistent from one region to the other. Therefore, different orientated grating patterns with 150 nm line-width and 300 nm pitch were achieved in the uneven PMMA on the whole FPA chip, as show figure 3(h). No difference in the PMMA thickness was observed for the 320 × 256 pixelated FPAs with the sample length of 2.2 cm, and regional exposure was not necessary.

After the replication of equal lines/spaces in PMMA with high quality, as presented in figure 3(h), a 100 nm thick Al film was then deposited by thermal evaporation in a high vacuum system, supplied by Kurt J. Lesker Ltd (Nano 36). The unwanted Al on the top of PMMA was washed away by a lift-off process in warm (60 °C) acetone for 30 min. The fabricated chips integrated with polarizers are presented in figure 4. If the pixels of the polarimeter were not perfectly orthogonal, the modulation of the incident light would have been strongly affected. In this work, the locations of both the sensing areas and alignment marks were simultaneously determined by the mask aligner (UV exposure). Based on the prefabricated marks, the polarizer was then precisely aligned with the InGaAs/InP FPA by using the registration system of the JEOL 6300 FS beam writer. The alignment error of the polarizer at both the *x*- and *y*-directions was well controlled within 6 nm, giving rise to high accuracy estimation of Stokes parameters, as shown in figure 4(d). Furthermore, the identical 150 nm line-width (figure 4(f)) on each pixel with different orientations of 0°, 45°, 90°, or 135° ensured an approximately equal relative throughput/transmission of incident infrared light, which is helpful to improve imaging quality.

3.2. *The effect of LER on the extinction ratio*

As mentioned above, poor extinction ratios lead to cross-talk at adjacent pixels. In this work, it was found that the LER of the fabricated metallic grating can directly influence the extinction ratio of the polarizer. The LER on the fabricated samples was measured using ProSEM software, supplied by GenlSys Ltd. Figure 5(a) shows the LERs of 37.5 nm and 6.7 nm, which were formed during the PMMA development process at 0 °C and 23 °C, respectively. Developing at relatively high temperature helps to reduce the line width fluctuation as well as the LER. Figure 5(b) presents the comparison of the extinction ratios from the two Al gratings with different LER in near infrared wavelength, calculated by the finite difference time domain (FDTD) simulation method. Here, the extinction ratio based on the simulation results was the ratio of transverse magnetic-polarized wave transmittance to transverse electric-polarized wave transmittance. Clearly, a low LER of grating is beneficial to the extinction ratio for polarization imaging, which was further confirmed by the measured results, as shown in figure 5(c).

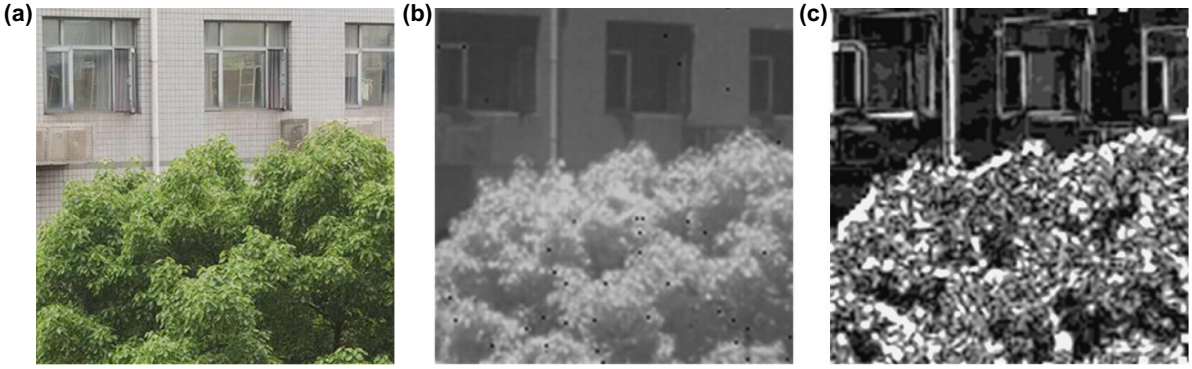

Figure 6. Comparisons of imaging quality by (a) CMOS imaging sensor at daytime, (b) conventional InGaAs detector, and (c) integrated InGaAs/InP FPA with grating-based polarizers in the dark.

3.3. Polarimetric imaging by the fabricated FPAs in infrared wavelengths

The staring imaging performance of the photoelectronic chip integrated with Al gratings was characterized, as presented in figure 6. The imaged scene, which was about 50 m away from the camera, consisted of plants and artificial buildings. It was clearly observed that the fabricated polarimetric InGaAs/InP FPA in this work shows significantly enhanced contrast in the image, compared to those images by a CMOS imaging sensor (figure 6(a)) as well as a prefabricated conventional InGaAs detector (figure 6(b)), which is important for promoting the target recognition capacity.

4. Conclusions

In this work, an important milestone was successfully established, i.e. the successful scaling up of the monolithic integration of grating-based polarizers to FPAs of InGaAs/InP detectors up to 540 × 4 pixels and 320 × 256 superpixels. Such an advance involves breakthroughs in a number of fundamental technical problems, including the effects of misalignment, LER of gratings, and the line width fluctuation on the extinction ratio of the fabricated polarimetric detector, which was closely related to the imaging contrast. To address these problems, novel nanoscale processes were developed. First, an irregular wafer-friendly mounting facility was developed to achieve highly precise alignment in the integration process. Second, the effect of the LER on the reduction of the extinction ratio was both theoretically studied and experimentally characterized, which was instructive in our effort to reduce the LER in the EBL process. Third, a regional e-beam exposure strategy was applied to effectively eliminate the effect of the chip shape irregularity on the line-width variation arising from the nonuniform PMMA thickness. Finally, the orientation-related deviations of the grating line-width caused by the intrinsic difference in the grid density between the orthogonal and the diagonal write were also avoided by adjusting the exposure dose accordingly. Therefore, the technique established in this work should be applicable to scale up photoelectronic chips with even higher integrity for high quality polarimetric imaging.

Acknowledgments

This work was financially supported by the following projects: Open project of SITP (Project Number: IIMDKFJJ-18-09); National Natural Science Foundation of China (Project Number: 61927820); The STCSM2019-11-20 funding (Project Number: 19142202700); National Natural Science Foundation of China (Project Number: NSF No. U1732104) and Zhejiang Lab's International Talent Fund for Young Professionals.

Conflicts of interest

The authors declare no conflict of interest.

Authors' contributions

B F, Y C and T L planned the projects and designed the experiments. B F and Z Y carried out the experiments. B F, D S, X L, T L and B Y analyzed the data; and B F wrote and edited the paper. Y C initiated the research topic and supervised the entire research. All authors read and approved the final manuscript.

ORCID iD

Yifang Chen https://orcid.org/0000-0002-5746-2762

References

[1] Shiraishi K, Oyama S and Tsai C S 2011 A polarizer using thin metallic-film subwavelength grating for infrared to terahertz region *J. Lightwave Technol.* **29** 670–6
[2] Liang J, Ren L Y, Qu E S, Hu B L and Wang Y L 2014 Method for enhancing visibility of hazy images based on polarimetric imaging *Photon. Res.* **2** 38–44
[3] Andreou A G and Kalayjian Z K 2002 Polarization imaging: principles and integrated polarimeters *IEEE Sens. J.* **2** 566–76
[4] Rubin N A, D'Aversa G, Chevalier P, Shi Z J, Chen W T and Capasso F 2019 Matrix Fourier optics enables a compact full-Stokes polarization camera *Science* **365** eaax1839

[5] Tyo J S, Goldstein D L, Chenault D B and Shaw J A 2006 Review of passive imaging polarimetry for remote sensing applications *Appl. Opt.* **45** 5453–69
[6] Chu J K, Wang Z W, Zhang Y J, Liu Z and Wang Y L 2013 Integrated blue-sensitive polarization-dependent photodetector *J. Micro/Nanolith. MEMS MOEMS* **12** 033005
[7] Gruev V, Perkins R and York T 2010 CCD polarization imaging sensor with aluminum nanowire optical filters *Opt. Express* **18** 19087–94
[8] Ikeda S, Higurashi E, Suga T and Oguchi T 2014 Miniaturized polarization sensors integrated with wire-grid polarizers *Proc. 2014 Int. Conf. Electronics Packaging (ICEP)* Toyama (Piscataway, NJ: IEEE) pp 376–379
[9] Nordin G P, Meier J T, Deguzman P C and Jones M W 1999 Micropolarizer array for infrared imaging polarimetry *J. Opt. Soc. Am.* A **16** 1168–74
[10] Baker G, Wilson M and Coulter P 2007 Development and results of NIR polarization camera *Proc. SPIE* **6567** 65671L
[11] Gruev V, Ortu A, Lazarus N, Van Der Spiegel J and Engheta N 2007 Fabrication of a dual-tier thin film micropolarization array *Opt. Express* **15** 4994–5007
[12] Tyo J S 2006 Hybrid division of aperture/division of a focal-plane polarimeter for real-time polarization imagery without an instantaneous field-of-view error *Opt. Lett.* **31** 2984–6
[13] Zhang Z G, Dong F L, Cheng T, Qiu K, Zhang Q C, Chu W G and Wu X P 2014 Nano-fabricated pixelated micropolarizer array for visible imaging polarimetry *Rev. Sci. Instrum.* **85** 105002
[14] Gilboa E, Cunningham J P, Nehorai A and Gruev V 2014 Image interpolation and denoising for division of focal plane sensors using Gaussian processes *Opt. Express* **22** 15277–91
[15] Vorobiev D and Ninkov Z 2015 Design, fabrication and characterization of a polarization-sensitive focal plane array *Proc. SPIE* **9403** 94030A
[16] Miller D A, Dereniak E L and Wilson D W 2012 Novel design and alignment of wire-grid diffraction gratings on a visible focal plane array *Opt. Eng.* **51** 014001
[17] York T and Gruev V 2012 Characterization of a visible spectrum division-of-focal-plane polarimeter *Appl. Opt.* **51** 5392–400
[18] Perkins R and Gruev V 2010 Signal-to-noise analysis of stokes parameters in division of focal plane polarimeters *Opt. Express* **18** 25815–24
[19] Sun D, Li T, Yang B, Shao X M, Li X and Chen Y F 2019 Research on polarization performance of InGaAs focal plane array integrated with superpixel-structured subwavelength grating *Opt. Express* **27** 9447–58
[20] Sun D, Feng B, Yang B, Li T, Shao X M, Li X and Chen Y F 2020 Design and fabrication of an InGaAs focal plane array integrated with linear-array polarization grating *Opt. Lett.* **45** 1559–62
[21] Xu C *et al* 2019 Integrating subwavelength polarizers onto InP-$In_xGa_{1-x}As$ sensors for polarimetric detection at short infrared wavelength *Photonics Nanostruct. Fundam. Appl.* **33** 10–15
[22] Wang R, Li T, Shao X M, Li X, Huang X Q, Shao J H, Chen Y F and Gong H M 2015 Subwavelength gold grating as polarizers integrated with InP-based InGaAs sensors *ACS Appl. Mater. Interfaces* **7** 14471–6
[23] Yang Z Y, Feng B, Lu B R, Chen Y F, Li W H, Zhang W and Li T 2020 Optimization study of metallic sub-wavelength gratings as the polarizer in infrared wavelengths *Appl. Opt.* **59** 1253–8
[24] Yang Z Y, Feng B, Lu B R, Chen Y F, Li W H, Zhang W and Li T 2020 A study of nano-structural effect on the polarization characteristics of metallic sub-wavelength grating polarizers in visible wavelengths *Microelectron. Eng.* **227** 111327
[25] He W, Shao X M, Ma Y J, Cao G Q, Chen Y, Li X and Gong H M 2019 Broadband high quantum efficiency InGaAs/InP focal plane arrays via high precision plasma thinning *Opt. Lett.* **44** 6037–40